

Atomic Force Microscope Image Contrast Mechanisms on Supported Lipid Bilayers

James Schneider, Yves F. Dufrêne, William R. Barger, Jr., and Gil U. Lee

Chemistry Division, Code 6170, Naval Research Laboratory, Washington, DC 20375-5342 USA

ABSTRACT This work presents a methodology to measure and quantitatively interpret force curves on supported lipid bilayers in water. We then use this method to correlate topographic imaging contrast in atomic force microscopy (AFM) images of phase-separated Langmuir-Blodgett bilayers with imaging load. Force curves collected on pure monolayers of both distearoylphosphatidylethanolamine (DSPE) and monogalactosylethanolamine (MGDG) and dioleylethanolamine (DOPE) deposited at similar surface pressures onto a monolayer of DSPE show an abrupt breakthrough event at a repeatable, material-dependent force. The breakthrough force for DSPE and MGDG is sizable, whereas the breakthrough force for DOPE is too small to measure accurately. Contact-mode AFM images on 1:1 mixed monolayers of DSPE/DOPE and MGDG/DOPE have a high topographic contrast at loads between the breakthrough force of each phase, and a low topographic contrast at loads above the breakthrough force of both phases. Frictional contrast is inverted and magnified at loads above the breakthrough force of both phases. These results emphasize the important role that surface forces and mechanics can play in imaging multicomponent biomembranes with AFM.

INTRODUCTION

In addition to its barrier function, the cell membrane plays an active role in cellular processes, including the controlled transport of ions and proteins into and out of the cell (Voet and Voet, 1990), transduction of extra- and intracellular signals (Berridge and Irvine, 1984), and mediation of cell-cell and cell-matrix adhesion (Hammer and Tirrell, 1996). The development of a molecular-level understanding of membrane/water interfacial chemistry has been complicated by the difficulty of applying surface spectroscopy techniques to fragile tissue samples in biologically relevant media. This understanding could lead to the rational design of effective drug delivery vehicles and improve the biocompatibility of synthetic surfaces. These complications can be circumvented in part by depositing lipid membranes onto solid supports for analysis using ellipsometry, infrared spectroscopy, reflectivity, and evanescent-wave excitation of membrane-associated fluorophors (McConnell et al., 1986; Sackmann, 1996). Amphiphilic constituents of cell membranes (Zasadzinski et al., 1991; Hui et al., 1995; Dufrêne et al., 1997; Vie et al., 1998), pulmonary tissue (Lipp et al., 1997; Discher et al., 1996; Nahmen et al., 1997), and the stratum corneum (Grotenhuis et al., 1996) have been deposited onto solid supports to assess their morphology and function under physiological conditions. Supported mem-

branes have also been explored for use as biosensors that rely on binding cells or ligands to cell-surface receptors (McConnell et al., 1986; Yu et al., 1997), often in conjunction with the electrical-insulating properties of the bilayer (Stelzle et al., 1993; Cornell et al., 1997; Plant, 1999).

The high spatial resolution of the atomic force microscope (AFM) has made it an important tool for imaging supported lipid and fatty acid layers at the submicron scale. The molecular-level order of fatty acid monolayers (Blackman et al., 1990; Hansma et al., 1991; Schwartz et al., 1992; Chi et al., 1993; Schaper et al., 1993) and lipid bilayers (Weisenhorn et al., 1991; Zasadzinski et al., 1991; Hui et al., 1995) has been precisely measured to assess defect formation and stability under different conditions. AFM has also been used to image the mesoscale structure of phase-separated planar fatty acid (Overney et al., 1992; Koleske et al., 1997; Chi, 1999) and lipid films (Solletti et al., 1996; Grotenhuis et al., 1996; Nahmen et al., 1997; Vie et al., 1998; Meine et al., 1998; Leporatti et al., 1998) as a means of visualization to complement Brewster angle microscopy and fluorescence microscopy. The shapes of adsorbed hemimicelles and more complicated microstructures have been measured by non-contact imaging based on electrostatic repulsion between probe and sample (Manne et al., 1994; Manne and Gaub, 1995). Because typical contact-mode AFM images are obtained at a constant probe-sample interaction force set point, the features observed are a direct result of the strength of local probe-sample interactions. Interpretation of the AFM images collected on supported lipid bilayers in water requires an understanding of the contribution of probe-sample surface forces and mechanical deformation at various imaging set points.

Changes in the probe-sample interaction force as the probe approaches the sample provide substantial information about the forces felt between the probe and the supported bilayers. This information is found by collecting and

Received for publication 6 January 2000 and in final form 16 May 2000.

J. S.'s current address: Department of Chemical Engineering, Carnegie Mellon University, 5000 Forbes Ave., Pittsburgh PA 15213-3890.

Y. F. D.'s current address: Unite de Chimie des Interfaces, Universite Catholique de Louvain, Place Croix du Sud 2/18, B-1348 Louvain-la-Neuve, Belgium.

Address reprint requests to Gil U. Lee, School of Chemical Engineering, Purdue University, West Lafayette, IN 47907-1283. Tel.: 765-494-4057; E-mail: gl@atum.ecn.purdue.edu.

© 2000 by the Biophysical Society

0006-3495/00/08/1107/12 \$2.00

analyzing AFM force curves. In principle, the strength of electrostatic (Butt, 1991a,b) and hydration (Ho et al., 1998) forces between probe and sample, as well as the mechanical deformation of probe and sample (Domke and Radmacher, 1998) can be identified by fitting features of the force curve to theoretical models that predict force as a function of probe-sample separation distance. However, because the AFM does not make an absolute measurement of probe-sample separation distance, the position of the probe with respect to a fixed reference must be specified at some point in the force curve. We address this issue (Dufrene et al., 1997, 1998) by measuring the differences in height, force, and adhesion across domains of phase-separated lipid bilayers, with one domain serving as a reference.

Here, we present a methodology to collect and analyze AFM force curves that establishes a reliable distance reference for force curves measured on supported lipid bilayers in water. The validity of the method is demonstrated by comparing differences in topography measured in contact-mode AFM images of phase-separated lipid bilayers in water to distance scales of force curves measured on their pure components. Bilayers are prepared on mica by Langmuir-Blodgett (LB) deposition of a desired monolayer onto a monolayer of the phospholipid distearoylphosphatidylethanolamine (DSPE). Pure monolayers of DSPE, dioleoylphosphatidylethanolamine (DOPE), and monogalactosyldiglyceride (MGDG) were each deposited onto DSPE monolayers on mica for force curve measurements. The force curves show an abrupt breakthrough of the bilayer at a repeatable, material-dependent force. The breakthrough forces for DSPE on DSPE and MGDG on DSPE are sizable, whereas those for DOPE on DSPE are too small to measure. Topography images of phase-separated, mixed bilayers of DSPE/DOPE on DSPE show a high topographical contrast at imaging set points below the breakthrough force for DSPE, and low contrast above the DSPE breakthrough force. At this high load, the domain boundaries are still clearly evident in friction, verifying their presence in the sample. Similar results are observed for images of MGDG/DOPE on DSPE. We show that the molecular mechanism responsible for the contrast observed in these systems at low loads is a selective puncturing of the DOPE domains by the AFM probe.

These effects are probably also seen when other lipid layers are probed, and a few examples exist in the literature (Blackman et al., 1990; Radler et al., 1994; Ducker and Clarke, 1994). This study cautions that AFM height imaging alone cannot rule out phase separation in multicomponent lipid bilayers, because the imaging contrast can be a strong function of imaging load. When collected and analyzed using our methods, AFM force curves provide a guide for choosing the set point appropriate for imaging multicomponent lipid bilayers in water. They also provide a powerful, quantitative probe of membrane/water interfacial chemistry.

EXPERIMENTAL METHODS

The lipids used in this study, DSPE, MGDG, and DOPE, were purchased from Matreya, Inc. (Pleasant Gap, PA) and Sigma (St. Louis, MO). Their purity was confirmed by electrospray mass spectroscopy. All lipids were dissolved at 0.5 mg/ml in a 4:1 mixture of high performance liquid chromatography grade chloroform and methanol. Triply distilled water was used for all measurements and cleaning procedures. LB films were deposited onto freshly cleaved mica by using a thermostated (25°C), computer-controlled LB trough (KSV 5000, KSV Instruments, Helsinki, Finland) which monitors surface pressure (Π) using a Wilhelmy plate. A DSPE monolayer was first deposited on the mica substrate on the upstroke by the following procedure. Coupons of mica (1 cm²) were submerged in the water subphase and a DSPE solution was added dropwise to the water surface. After 5 min, the film was compressed to 25 mN/m at 1 mN/min and deposited on the upstroke (5 mm/min). The monolayer of interest (DSPE, MGDG, DOPE, or a mixture thereof) was subsequently deposited onto the DSPE monolayer at $\Pi = 25$ mN/m and 5 mm/min on the downstroke. The bilayer-covered mica coupons were transferred under water to the AFM.

The AFM cantilevers used in this study had a nominal spring constant of 0.5 N/m and the probe was coated with a hydrophilic monolayer (Dufrene et al., 1998). Chips of oxide-sharpened siliconoxynitride probes (Thermomicroscopes, Sunnyvale, CA) were coated in a high-vacuum, electron beam thermal evaporator (CVC Products, Inc., Rochester, NY) with a 4-nm chromium adhesion layer and 60-nm gold layer. The chips were rotated during deposition to apply metal to both sides of the cantilever and minimize the effect of stress in the deposited films. The probes were functionalized with a hydrophilic self-assembled monolayer by immersion in a 10- μ M ethanolic solution of mercaptohexadecanol for several hours. Before use each chip was rinsed in pure ethanol and water and mounted in a cleaned fluid cell. Gold-coated silicon wafers co-incubated with the AFM probes have very low contact angles with water ($<5^\circ$), which is consistent with the formation of well-ordered monolayers (Bain et al., 1989).

AFM measurements were carried out at $25 \pm 5^\circ\text{C}$ using a commercial instrument (Nanoscope IIIa, Digital Instruments, Inc., Santa Barbara, CA) with an optical lever detector. A silicon O-ring was rinsed in ethanol, dried, and placed onto the mica substrate in the transfer beaker. Using clean stainless steel tweezers, the mica and O-ring were lifted from the beakers and placed onto the AFM scanner. The AFM cantilever chip was mounted onto a liquid cell and carefully lowered onto the O-ring, sealing it between the cell and substrate. After waiting 1 hour for thermal and mechanical equilibration, AFM images were acquired in constant deflection mode to verify the composition and cleanliness of the surfaces. No changes in the images or force data were observed up to 14 h after deposition, ruling out bilayer depletion effects over the time course of this experiment.

Force curves were acquired in a 16×16 array, each with 1024 data points, over a $1\text{-}\mu\text{m}^2$ region that was not previously contacted. A triggering mechanism initiated retraction after 150 nm of cantilever deflection or about 75 nN of load. The radius of curvature R of the probes was measured by imaging a nanofaceted SrTiO₃ crystal (Shieko et al., 1993). Spring constants k were determined by calibration against a second, micro-machined cantilever of precisely controlled stiffness (Tortones and Kirk, 1997). The spring constants for cantilevers with similar dimensions did not vary more than 10% from the mean value for each cantilever.

The detector and piezo signals (Fig. 1 A) were converted to force-displacement curves using the algorithm outlined below. The piezo response (z) was independently measured as a function of applied voltage at several slow rates using a capacitance displacement sensor (Capacitec, Boston, MA). Using this calibration, piezo hysteresis (and, to a limited extent, creep) were fitted using a second-order polynomial expression. The detector sensitivity S , in V/nm, was determined by equating it to the slope of the force curve in the high load region between 2.0 and 4.0 V. The accuracy of this calibration depends on the assumption that there is minimal deformation of the probe and surface in the high load region. In some cases, erratic data were observed in the high load region because of

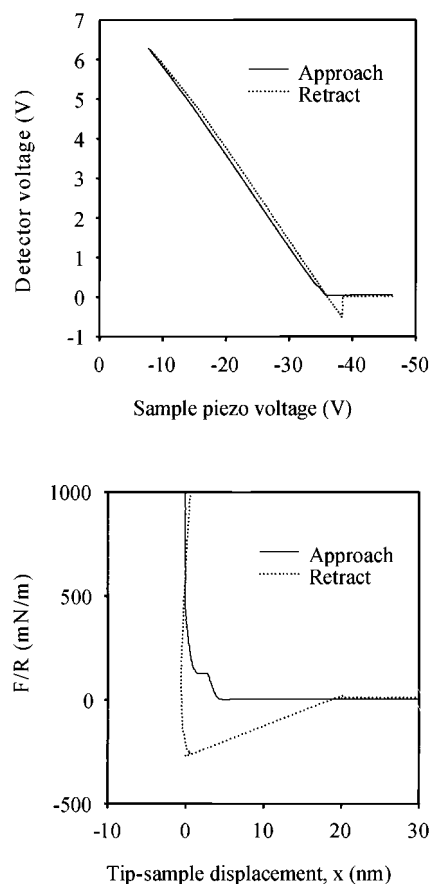


FIGURE 1 Detector signal vs. sample piezo voltage (A) and normalized force (F/R) versus probe-sample displacement x (B) force curves for probing DSPE monolayers on DSPE monolayers in water with a modified AFM probe. Bold lines are probe approach traces, and dotted lines are retract traces. The raw voltage data were offset to a value of 0 V in the noncontact region of the plot. The data between 2.0 and 4.0 V serve as a calibration regime in which the probe remains at the same depth in the sample.

cantilever buckling (Hoh and Engel, 1993) and were disregarded. The probe-sample force F was calculated from the displacement of the cantilever d , assuming first-order Hookean behavior.

The AFM does not measure absolute probe-sample separation distance D . Rather, it measures relative changes in the probe-sample separation x' , the distance between the base of the AFM probe and the base of the substrate (Fig. 2). Using the point of highest loading as a reference, the following relationship must be obeyed:

$$x' - x'_0 = (d - d_0) - (z - z_0), \quad (1)$$

where the subscript $_0$ refers to the value obtained at the point of highest loading. The probe-sample displacement x is the difference between the probe-sample separation at a specific load x' and at the point of highest loading x'_0 :

$$x = (d - d_0) - (z - z_0), \quad (2)$$

Fig. 1 B shows a force-displacement curve produced by these transformations when using raw data (Fig. 1 A) collected while probing DSPE monolayers on DSPE in water. Note that changes in D and deformation effects are embodied in x .

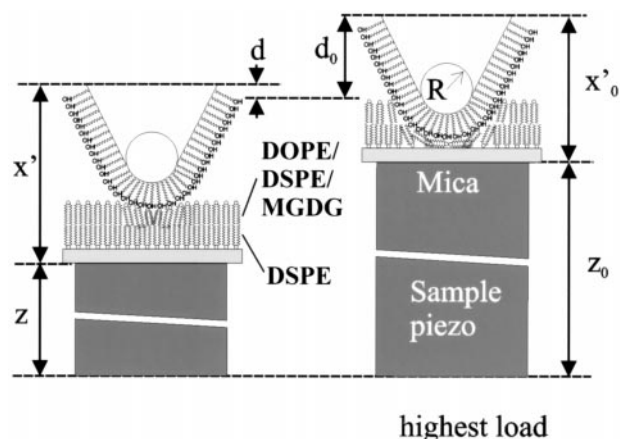


FIGURE 2 Geometry of the interaction between alkanethiol-SAM-modified AFM probe and LB bilayers on mica when out of contact and at the point of highest loading. The curved shape of the AFM probe apex can be modeled as a sphere of radius R . A monolayer of DSPE, MGDG, DOPE, or a mixture thereof is deposited onto a monolayer of DSPE in the configuration shown. The probe-sample displacement x is the distance between the base of the AFM probe and the base of the sample, and is a function of the probe-sample separation distance D and penetration of the probe into the sample. The probe-sample displacement x is set to zero at the point of highest loading (see Experimental Methods).

RESULTS

We present an approach to analyzing AFM force curves on lipid bilayers in aqueous systems that produces force curves whose distance scales correlate with topographical features in AFM images. A major difficulty in reaching this goal is the observation that probe-sample interaction forces are greatly affected by the variations in shape and surface chemistry of commercial AFM probes (Lee et al., 1996). To minimize these effects, AFM probes used in this study are modified with self-assembled monolayers of 1-mercaptohexanol. We have also measured the radius of curvature of the probe apex and scaled the applied load by the radius to account for probe curvature effects, as we describe in the next section. Fig. 2 illustrates the modified probe.

The lipid bilayers we investigate are constructed by a two-step LB deposition process to produce surfaces of defined chemistry and mechanical properties. First, freshly cleaved mica is rendered hydrophobic by depositing a monolayer of DSPE (Fig. 3 A) on the upstroke at a surface pressure of 25 mN/m. The monolayer of interest (DSPE, MGDG, DOPE, or mixtures thereof) is subsequently deposited onto the DSPE monolayer on the downstroke at 25 mN/m. The result is a composite bilayer on mica, with the headgroups of the lipid of interest facing the aqueous medium (Fig. 2). The 18-carbon dialkyl phospholipid DOPE (Fig. 3 C) has a single degree of unsaturation in each tail, which encumbers its close packing in Langmuir monolayers. That is demonstrated by its pressure-area isotherm, which is a liquid-expanded (LE) phase at all surface pres-

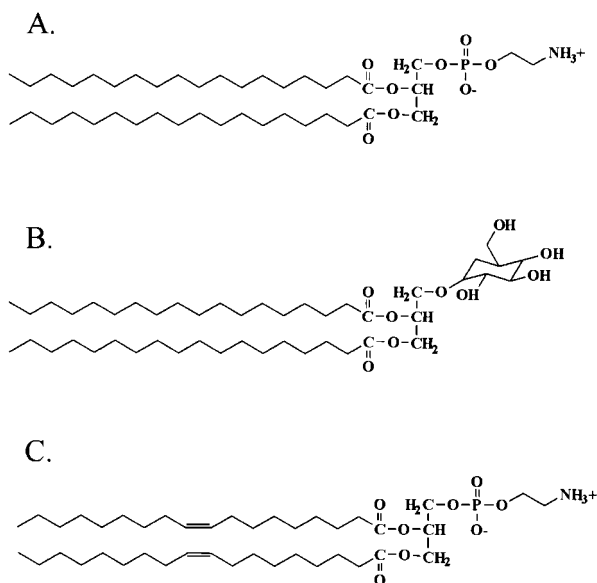


FIGURE 3 Chemical structures of the lipids studied here. DSPE (A) and MGDG (B) have fully saturated dialkyl tails, whereas DOPE (C) has one degree of unsaturation in each tail.

tures (Fig. 4). Both DSPE and MGDG (Fig. 3 B) have 18-carbon, fully saturated dialkyl tails, and their monolayers are compressed into the liquid-condensed (LC) phase at surface pressures above 5 mN/m (Fig. 2). Mixtures of the saturated lipids and DOPE have been observed to phase-separate into islands of saturated lipid surrounded by DOPE (Dufrêne et al., 1997).

Forces on lipid bilayers

AFM force curves are often used as a guide to determine the imaging load, also called the set point. Fig. 1 A shows a raw

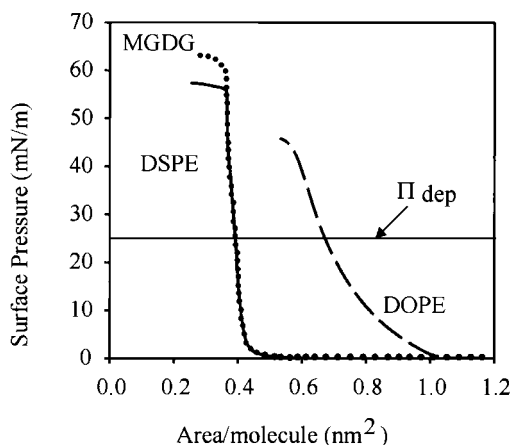


FIGURE 4 Pressure-area isotherms for DSPE, MGDG, and DOPE on a pure water subphase ($T = 25^\circ\text{C}$). At the deposition pressure ($\Pi_{\text{dep}} = 25$ mN/m), the DSPE and MGDG are in the LC phase, and the DOPE is in the LE phase.

force curve collected on a DSPE monolayer on DSPE in water. The DSPE force curves show a small jump-in on the loading part of the curve, and a moderate adhesion is measured as the probe is extracted from the sample. The range of the jump-in is more clearly demonstrated by plotting the data as scaled force F/R vs. probe-sample displacement x (Fig. 1 B). The probe-sample displacement is the difference between the separation distance of probe base and sample base at a given load and at the point of highest loading (Fig. 2). As such, x decreases as the probe approaches the sample (decreasing the probe-sample separation distance D) or penetrates the sample.

Fig. 5 shows approach force-displacement curves for the three lipid systems (DSPE, MGDG, and DOPE) monolayers on DSPE monolayers. The jump-in events are evidenced by a large spacing between the data points, indicating abrupt movements of the cantilever. The distance over which the jump-in occurs is about 2 nm for DSPE and MGDG, and about 3.5 nm for the DOPE. The force required for jump-in varies substantially for the three systems. Statistical analysis of a 256 force curve shows that the jump-in occurs at indistinguishably small loads for the DOPE, at $F/R = 105 \pm 15$ mN/m for the DSPE, and at $F/R = 220 \pm 10$ mN/m for the MGDG. The repulsive force curve on DSPE at $100 \text{ mN/m} > F/R > 10 \text{ mN/m}$ has been found to be consistent with the elastic deformation of the lipid bilayers and short-range surface forces (Dufrêne et al., 1998). As a result, the charge-neutral probe appears to be in contact with the charge-neutral surface at loads above $F/R = 10$ mN/m, and the ~ 2 -nm jump-in must involve an abrupt post contact puncturing of the LC lipid bilayers. We refer to the load at which the jump-in occurs as the breakthrough force. Similar post-contact jump-in events have been observed between

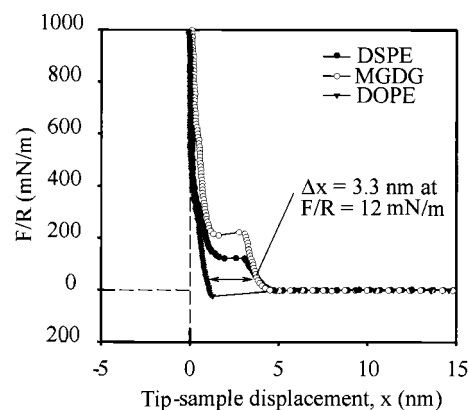


FIGURE 5 Force-displacement curves for probing DSPE, MGDG, and DOPE monolayers on DSPE monolayers in water with the modified AFM probes. Symbols represent data regularly sampled during the approach of the probe. Lines are presented to guide the eye. Large spaces between the data points indicate abrupt jumps of the cantilever. The DSPE and DOPE curves are separated by 3.3 nm at $F/R = 12$ mN/m, the imaging load used for the images in Fig. 6.

depleted lipid bilayers using the surface-force apparatus (Helm et al., 1989, 1992; Marra and Israelachvili, 1985) and while probing fatty acid layers adsorbed onto silica using the AFM (Ducker and Clarke, 1994).

Imaging of phase-separated lipid bilayers

Fig. 6, *A* and *B*, shows $15 \times 15 \mu\text{m}$ AFM topography and friction images, respectively, of a 1:1 mixed monolayer of DSPE/DOPE on a DSPE monolayer, imaged at a scaled load of $F/R = 12 \text{ mN/m}$, well below the breakthrough force for DSPE ($F/R = 105 \text{ mN/m}$). A white circle has been placed in the lower right hand corner as a placeholder for future reference. Phase segregation is observed with three domains distinguishable in topography images in the form

of high, medium, and low domains. By varying the concentration of the components' monolayer, we have determined that the high domains are DSPE and the medium-height domains are DOPE (Dufrêne et al., 1998). The low domains are vacancies in the bilayers. They are likely formed as the underlying DSPE is locally exposed to water and desorbed during the reorganization of the DSPE-DOPE monolayer on deposition onto pure DSPE. The DSPE-DOPE monolayers deposited onto mica on the upstroke or onto tightly held hydrophobic alkanethiol SAM on the downstroke (Boland et al., 1999), do not have the lower domains and have very round separated lipid domain shapes, implicating the underlying DSPE monolayer in the reorganization. The presence of the vacancies does not appear to alter the surface chemistry of the DSPE and DOPE phases; force curves measured

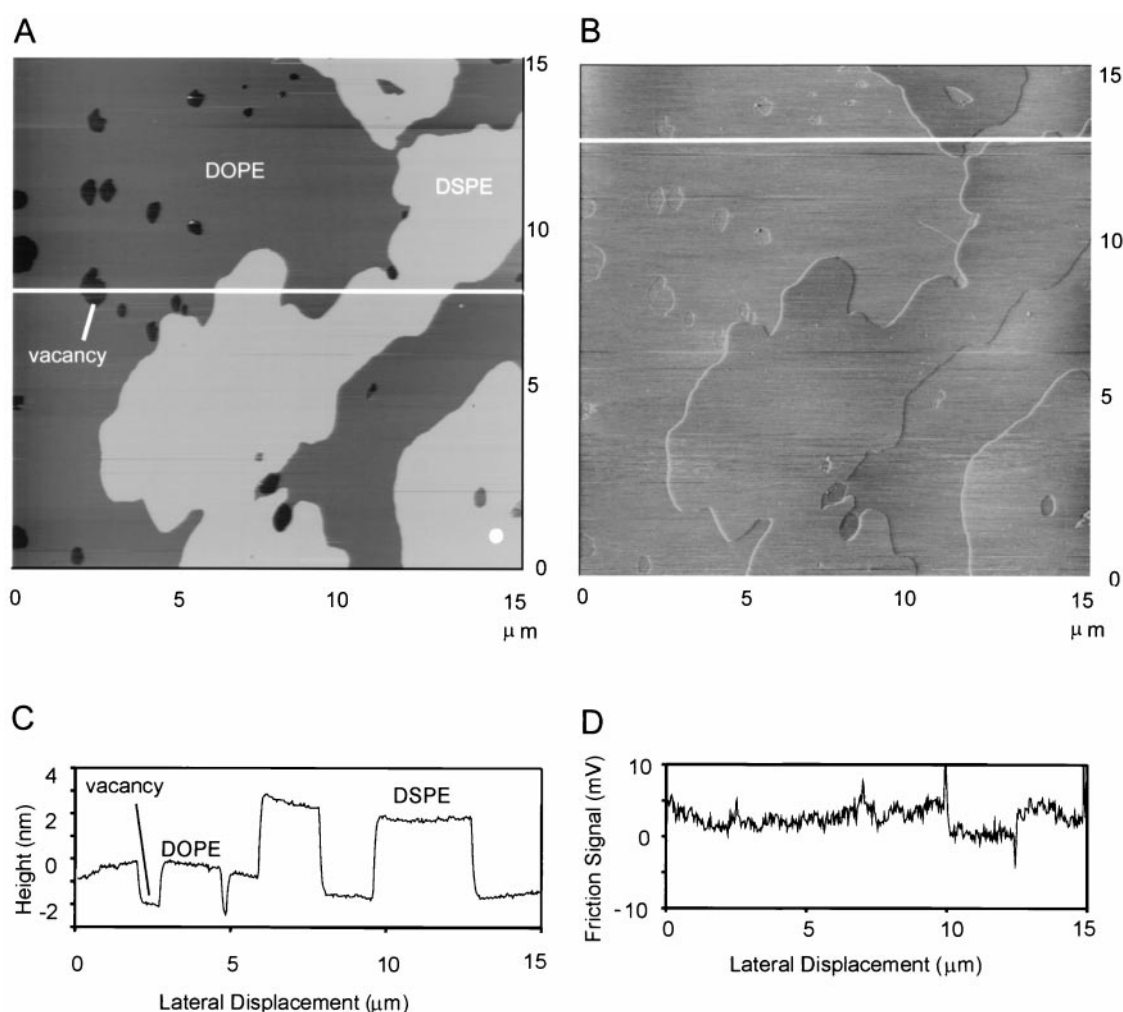


FIGURE 6 Topography (*A*) and friction (*B*) AFM images of 1:1 DSPE-DOPE mixed monolayers on DSPE monolayers in water imaged in contact mode at a scaled load of $F/R = 12 \text{ mN/m}$ (below the DSPE breakthrough force). The three domains distinguishable in (*A*) are labeled. A section analysis (*C*) for the topography image (*white line*) shows that the DSPE domains are $\sim 3.5 \text{ nm}$ above the DOPE domains and the vacancies are $\sim 1.6 \text{ nm}$ below the DOPE domains. A section analysis (*D*) of the friction image (*white line*) shows a higher friction force ($\sim 0.004 \text{ V}$) when scanning through the DOPE domains or vacancies. (All friction images presented were collected on the trace, and more positive friction signals correspond to higher frictional force.) A feature of the image is marked with a *white dot* for reference. Image sizes are $15 \times 15 \mu\text{m}$.

on the mixed monolayer compare favorably to those measured on pure monolayers. The size or number of the holes did not increase with time over a 24-hour period, as may be expected for a bilayer depletion mechanism (Helm et al., 1989, 1992; Marra and Israelachvili, 1985).

Cross-sectional analysis of the topographic image (Fig. 6 C) shows that the DSPE domains are 3.5 nm above the DOPE domain, which is significantly larger than the known thicknesses that would have been predicted from space-filling models. This height difference compares well with the difference in probe-sample displacement between the DSPE and DOPE force curves at this imaging load ($\Delta x = 3.3$ nm, Fig. 5). The DSPE domains are 5.1 nm above the low domains, approaching the thickness of a DSPE bilayer as measured by x-ray diffraction (6.4 nm; Seddon et al., 1984). The DOPE domains are only 1.6 nm above the vacancies, less than the thickness of a half-bilayer of DSPE

(3.2 nm). These results clearly indicate that on contact, the apex of the AFM probe penetrates the DSPE and DOPE domains to different degrees. The probe appears to deform the surface of the DSPE domains but to penetrate completely the DOPE domains into the tails of the underlying DSPE monolayer.

Fig. 6 D is a cross-section of the friction force image of the mixed DSPE and DOPE monolayer. It shows a slightly higher friction signal (0.004 V higher) when scanning through the DOPE phase. The higher friction on DOPE may be attributed to deeper probe penetration into the DOPE domains, giving rise the formation of additional probe-sample contact area (Dufrêne et al., 1997).

Strikingly, topography images of the same DSPE-DOPE monolayer collected at an imaging load of $F/R = 124$ mN/m (above the breakthrough force for DSPE) show an extinction of topographic contrast across domains (Fig. 7 A). A

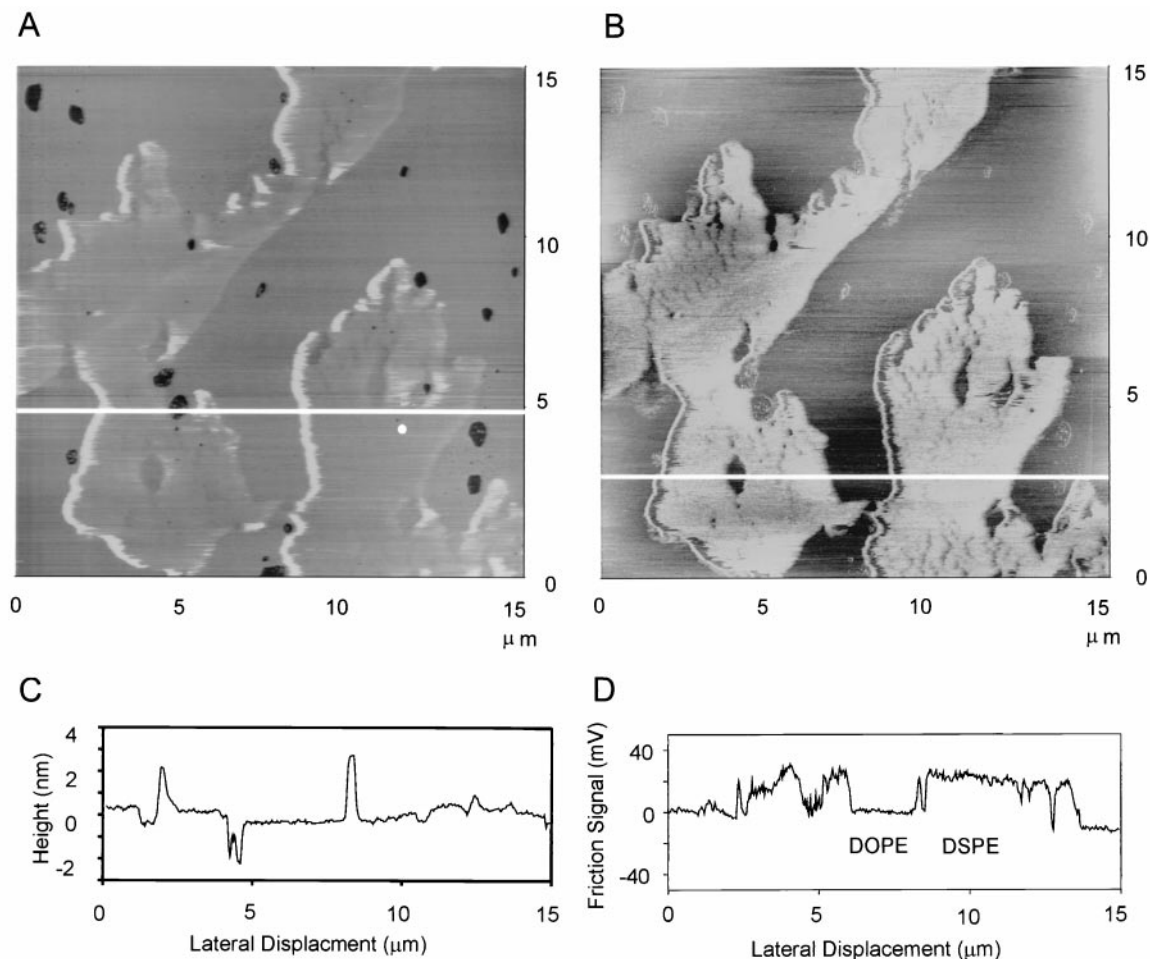


FIGURE 7 Topography (A) and friction (B) AFM images of the same sample region shown in Fig. 6 imaged in contact mode at $F/R = 124$ mN/m (above the DSPE breakthrough force). The DSPE domains of Fig. 6 A are barely visible in the topography image (A), but are very distinct in the friction image (B). A section analysis (C) for the topography image (white line) shows that the DSPE domains are ~ 0.3 nm above the DOPE domains and the vacancies are ~ 1.6 nm below the DOPE domains. A section analysis (D) of the friction image (white line) shows an inversion and enhancement of the friction signal compared to Fig. 6 C, with a much higher friction force (~ 0.025 V) when scanning through the DSPE domains. The white reference dot in (A) has shifted slightly due to thermal drift. Image sizes are 15×15 μm .

cross-section (Fig. 7 *D*) shows that the DSPE domains are only 0.6 nm higher than the DOPE domains at this high imaging load. Again, that is in good agreement with the difference in probe-sample separation distance ($\Delta x = 0.8$ nm) obtained from the force-displacement curves. The DOPE domains remain at 1.6 nm above the vacancies, indicating that the higher load has not compressed the DOPE any further. Another striking feature of high imaging loads is that the frictional contrast (Fig. 7, *B* and *D*) is increased and reversed for the DSPE and DOPE phases, with the penetrated DSPE domains showing the higher friction signal (0.025 V higher).

Returning the imaging load to a value below the breakthrough force restores the original topography and friction contrast. Fig. 8, *A* and *B*, shows contact-mode images of the same DSPE-DOPE monolayer on a DSPE monolayer collected at an imaging load of $F/R = 62$ mN/m, below the DSPE breakthrough force. Apart from some lateral drift of the sample, the original domains of Figs. 6 and 7 are distinguishable in both topography and friction. Surprisingly, very little damage is observed in the DSPE domains after the high-load imaging. A section analysis of the topography image (Fig. 8 *A*) and the friction image (Fig. 8 *B*) compares favorably with those of Fig. 6, *C* and *D*, again indicating that the original state of the mixed monolayer has not been significantly perturbed by the high-load imaging.

This strongly load-dependent topography contrast is not a special feature of the DSPE-DOPE system. Fig. 9, *A* and *B*, shows contact-mode AFM images of a 1:1 mixed monolayer of MGDG and DOPE on a DSPE monolayer obtained at an imaging load ($F/R = 170$ mN/m) below the MGDG breakthrough force ($F/R = 220$ mN/m). As for the DSPE-DOPE system, three domains are distinguishable in the topography and friction images. Comparison of adhesion data (not shown) identifies the high domains as MGDG and the medium-height domains as DOPE, along with the vacancies. Images of a sample prepared under identical conditions but imaged at $F/R = 290$ mN/m (above the breakthrough force for MGDG) also show a removal of topography contrast (Fig. 10 *A*) and an enhancement and reversal of frictional contrast (Fig. 10 *B*). In Fig. 10 *A*, the presence of the domains can be detected only by the absence of vacancies in the MGDG-covered regions of the image.

DISCUSSION

Image contrast mechanisms

Our results suggest that topographic and friction contrast mechanisms observed in the phase-separated lipid films are dominated by the abrupt penetration of lipid films at a repeatable, material-dependent F/R . Fig. 11 schematically presents a model for the mechanism of load-dependent topographic imaging contrast between the DSPE and DOPE domains. At low loads, a selective penetration of the DOPE

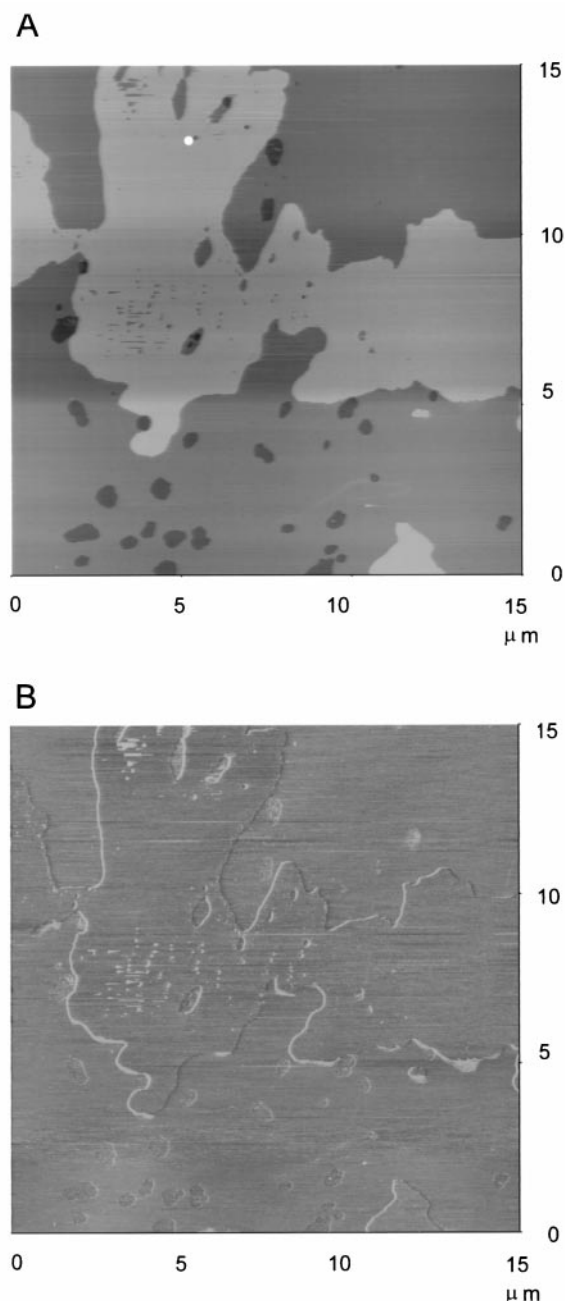


FIGURE 8 Topography (*A*) and friction (*B*) AFM images of the same sample region of Figs. 6 and 7 imaged in contact mode at $F/R = 64$ mN/m (below the DSPE breakthrough force) after the high-load imaging. The high contrast in topography (*A*) and the low contrast in friction (*B*) are restored with very little damage to the film. The white reference dot in (*A*) has shifted slightly due to sample drift. Image sizes are $15 \times 15 \mu\text{m}$.

phase occurs (Fig. 11 *A*) that produces a step height at least as large as the thickness of the DSPE monolayer. This imaging mode accounts for the large step height and image contrast reported for supported lipid bilayers (Dufrene et al., 1997). At higher loads, the breakthrough force of the DSPE monolayers is exceeded, resulting in the penetration of both

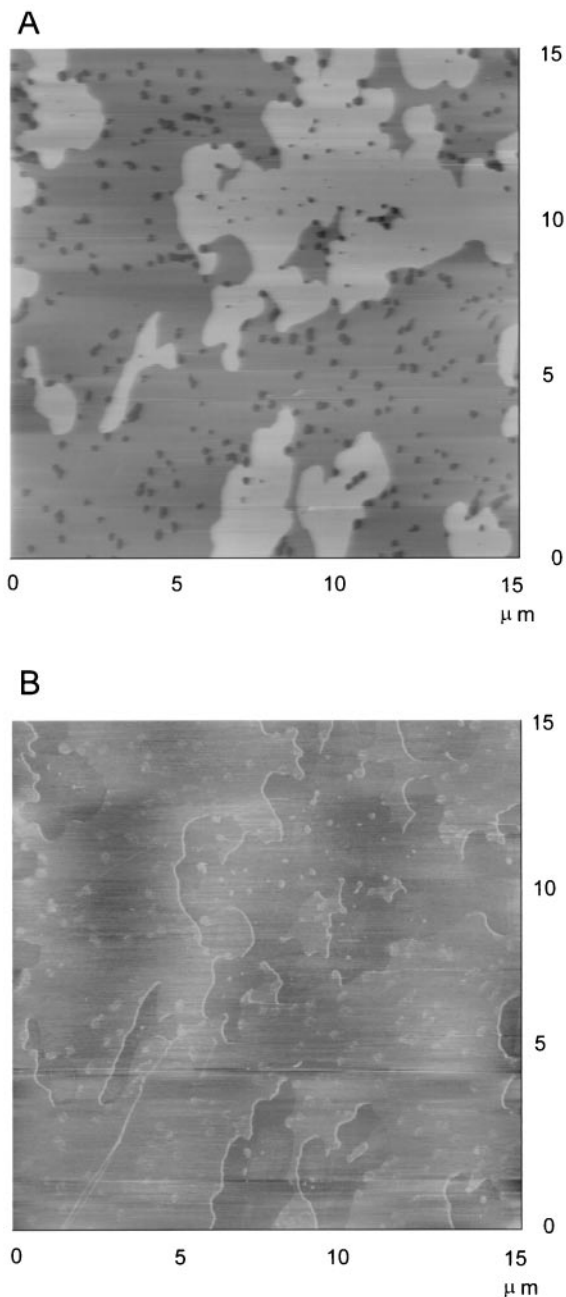


FIGURE 9 Topography (A) and friction (B) AFM images of a 1:1 mixed monolayer of MGDG-DOPE on a DSPE monolayer in water imaged in contact mode at $F/R = 170$ mN/m (below the MGDG breakthrough force). The three domains distinguishable in (A) are labeled. Image sizes are 15×15 μm .

domains and little topographic contrast between the two phases (Fig. 11 B). We were surprised that the aggressive, high-load imaging that led to penetration of DSPE did not greatly damage the film, particularly considering the deep penetration of the probe. Because the DSPE monolayers are able to reseal the furrow created by the AFM probe without major reorganization, it is possible that the lipids are never

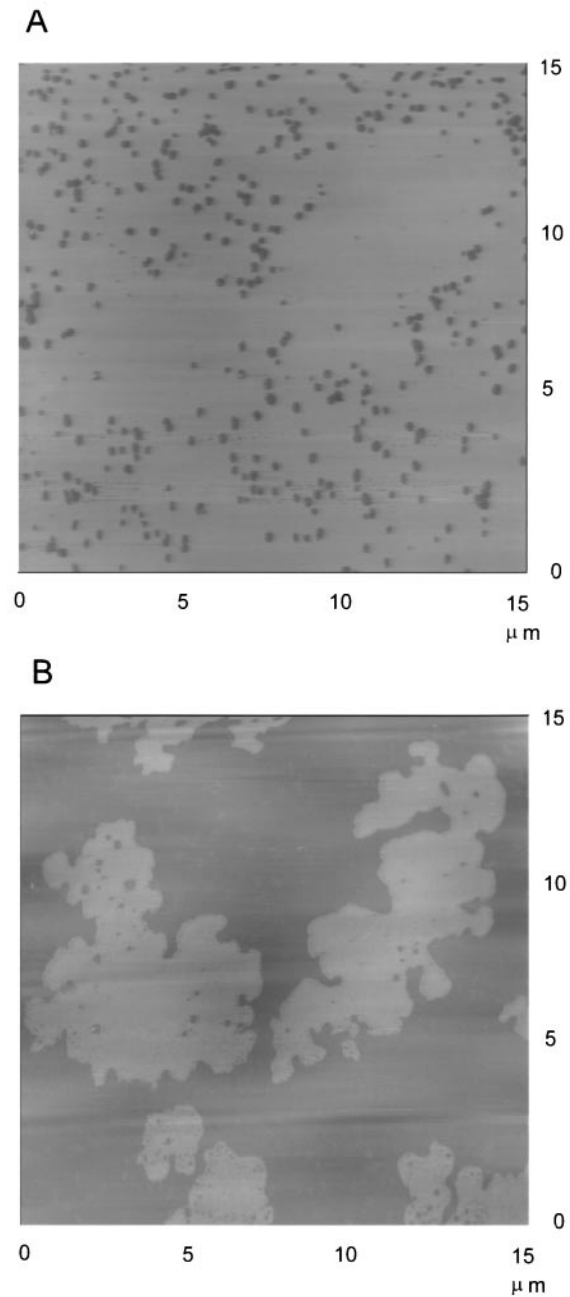


FIGURE 10 Topography (A) and friction (B) AFM images of another 1:1 mixed monolayer of MGDG-DOPE on a DSPE monolayer imaged in water at $F/R = 290$ mN/m (above the breakthrough force). Image size is 15×15 μm .

removed from the surface, only deformed locally in a reversible, elastic way.

A macroscopic description of a general tribological process predicts that the friction force F_f is dependent on both the area of contact A and critical shear stress S_c of the contact interface (Bowden and Tabor, 1967):

$$F_f = S_c A. \quad (3)$$

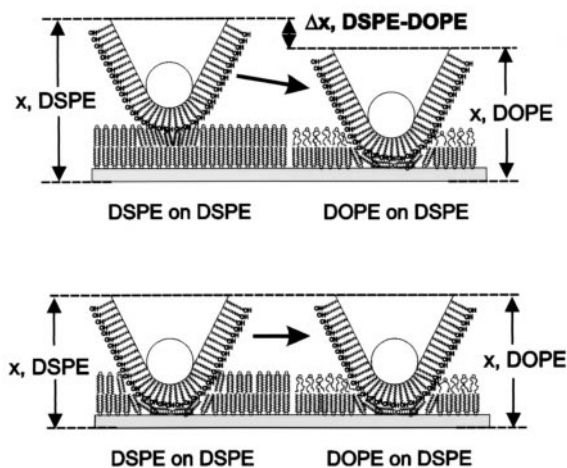


FIGURE 11 Depiction of AFM probe penetration while imaging DSPE-DOPE films at loads below (A) and above (B) the breakthrough force for DSPE.

The area of contact of the probe scales with the depth of probe penetration, whereas the critical shear stress is a material-dependent property that scales with the surface compressional modulus of the film. The surface compressional moduli of the DOPE and DSPE films in these bilayers are 79 and 183 mN/m, respectively (Dufrene et al., 1998). Within this simple model, at low imaging loads, the higher frictional force on the DOPE monolayer results largely from the large contact area of the probe with the DOPE phase (~ 3 times larger). At high loads, the probe penetrates both monolayers, and so the contact area is similar in both monolayers. Frictional contrast at high loads results from the high critical shear stress of the DSPE monolayer.

Table 1 summarizes the height differences across domains (step heights) and Δx data from force-displacement curves for the two lipid systems at various loads. These differences show the remarkable agreement between these two values supporting the model presented in Fig. 11. The force curve and image data can be matched to obtain a measurement of the bilayer thickness as well. Each of the

TABLE 1 Probe-sample displacement and step height

Monolayer	F/R (mN/m)	Δx (nm)	Step height (nm)
DSPE-DOPE	12	3.3 ± 0.4	3.5 ± 0.4
DSPE-DOPE	130	0.8 ± 0.4	0.6 ± 0.4
MGDG-DOPE	170	2.7 ± 0.4	2.8 ± 0.4
MGDG-DOPE	290	0.3 ± 0.4	~ 0

Summary of differences in probe-sample displacement Δx and differences in height (step height) between mixed-monolayer domains as a function of scaled load (F/R). Excellent agreement is observed between Δx and step height for these systems both above and below the breakthrough forces of DSPE ($F/R = 105 \pm 15$ mN/m) and MGDG ($F/R = 220 \pm 10$ mN/m). Uncertainties are based on statistical analysis of a series of force curves Δx and a bearing analysis of the images (step height).

force curves (Fig. 5) shows an onset of repulsive forces at $x = 4.5$ nm. Images of DOPE monolayers on DSPE taken at loads above $F/R = 2000$ mN/m (where $x = 0$ nm on the force curves) show vacancies at a depth of ~ 1.6 nm, and therefore, at $x = 0$ the probe is ~ 1.6 nm above the mica surface. The onset of measurable repulsive forces for the DSPE on DSPE force curves (Fig. 5) occurs at a distance of $4.5 + 1.6 = 6.1$ nm above the mica surface, which is in agreement with the DSPE bilayer thickness obtained from scattering data (6.4 nm). It should be noted that the precision of the absolute thickness measurement is limited by the measurement of the vacancy heights at high loads, about ± 0.2 nm. Taken together, these data clearly demonstrate that the force-displacement curves obtained using our method are a reliable measure of the absolute depth at which the probe resides within supported lipid bilayers at a particular load. This opens the door for the use of AFM force curves as a quantitative probe of membrane/water interfacial chemistry, a subject we will address in future publications.

These observations also send an important message for those using the AFM as a tool to image soft materials, such as cells or their molecular components: topographic and frictional contrast in AFM results from a convolution of load-dependent morphological and material properties. Indeed, the fairly high breakthrough forces measured in this study could easily be achieved during tapping-mode imaging of samples using ultrasharp probes. We suggest that a thorough analysis of AFM force curves collected over different areas of the sample be undertaken to determine the form of the surface forces or whether different breakthrough forces exist across the sample. Because of variations in AFM probe geometry and cantilever spring constants, we also suggest that this analysis include probe characterization of the type used here.

Force curve treatment and interpretation

The ability to measure accurately force and separation in surface force measurements is critical for characterizing complex systems, such as the lipid bilayers, in which a number of interactions can contribute to an observed behavior. Developing accurate AFM force measurements has been challenging because of the scale of the measurement. The force curves presented in Fig. 5 differ significantly from conventional AFM force curves in that their form is independent of the specific probe used. These improvements in force measurements have resulted from the scaling of force by the radius of curvature of the probe, the identification of a point of contact, and the control of the chemistry of the probe. The following discussion describes the rationale and assumptions associated for the scaling of the force by the radius of the curvature of the probe and the identification of a point of contact.

Scaling force by radius has been widely used in macroscopic surface force measurements that use the sphere-on-flat geometry. The AFM probe can be regarded as spherical only when sample penetration and the range of surface forces between probe and sample are much smaller than the probe curvature. The gold-coated probes we use here had curvatures on the order of 40 nm, whereas the penetration of the sample was less than 6 nm. The Derjaguin approximation (Derjaguin, 1934) allows the force between a sphere and flat F_s to be converted to an energy per unit area between parallel planes E_p :

$$F_s(D)/R = 2\pi E_p(D) \quad (4)$$

Derjaguin's approximation applies to many forms of interaction as long as the range of the interaction and the separation between the surfaces D are much less than the radius of the probe R . Fortunately, long-range electrostatic surface forces can be neglected in this study, since the probe and surface are both charge-neutral. Application of the Derjaguin approximation to the AFM data allows us to convert surface forces into surface energies and thus compare measurements with a wide range of probe sizes.

Our identification of a point of contact in the force curves of the loading of the bilayer by the modified probe depends on the assumption that there is a critical load above which insignificant change in the probe-sample displacement x occurs. The validity of this approximation is supported by experimental observation that the depth of the vacancies in the DOPE phase does not measurably decrease when imaging at ultrahigh loads. That is, topography images of mixed monolayers on DSPE in water imaged at $F/R = 2500$ mN/m show vacancy depths (1.9 nm) nearly identical to those measured at $F/R = 250$ mN/m. Because the bottom of the vacancies represents exposed mica, we conclude that the probe does not move significantly closer to the mica between $F/R = 250$ mN/m and $F/R = 2500$ mN/m, a force range that includes the calibration regime.

The physical basis for treating the deformation of the surface as negligible at $x = 0$ is based on the fact that the compliance of the AFM mechanical loop K is determined by the sum of its elements k_i :

$$1/K = \sum_i 1/k_i. \quad (5)$$

As a result, the most compliant components in the system (i.e., cantilever, probe, or sample) will dominate the compliance of the system. Young's moduli E of the probe and sample (Table 2) indicate that the most compliant material on the sample is the LB layer by at least an order of magnitude. The Young's moduli clearly explain why the monolayer of the lipid adjacent to the water is deformed by the probe. It can easily be shown that the deformation of the next most compliant material, the alkanethiol SAM on the probe, is very small. However, these parameters do not

TABLE 2 Comparison of Young's moduli for different materials

Material	Young's modulus, E (GPa)	Reference
Silicon nitride	192	Buchaillet et al., 1997
Gold	82	Stedfeld, 1979
16-carbon alkanethiol SAM	2	Salmeron et al., 1993
LB layer*	0.16	Dufrène et al., 1998
Muscovite mica	140	Stedfeld, 1979

Comparison of Young's moduli for the materials used in the deformation force curves.

*Obtained by a Hertzian fit to an AFM force curve obtained using a similar self-assembled monolayers-modified probe (see text).

explain the apparent stiffness of the inner monolayer adjacent to the mica. The increase in stiffness of the inner lipid monolayer results from the fact that the stress field generated by the probe extends into the stiff substrate as the probe indents the monolayer (Ogilvy, 1993; Radmacher et al., 1995). Macroscopic models of elastic layers on hard surfaces suggest that the substrate effects will dominate the mechanical response of the lipid monolayer at penetrations of 2 nm (Meijers, 1968). At this point, the sample stiffness exceeds the cantilever stiffness, and further movements of the sample piezo act only to deform the cantilever.

The success of this technique depends greatly on choosing the appropriate regime of the detector voltage versus sample piezo position curves to calibrate the detector and serve as a reference for the position of the probe at high loads. We have found that data between loads of $F/R = 1500$ mN/m and $F/R = 2000$ mN/m are most suitable for cantilevers with $k = 0.5 \sim 0.7$ N/m. Loads of $F/R = 1000$ to $F/R = 1500$ mN/m are necessary to place the probe at its ultimate location, yielding a linear detector voltage versus piezo position curve and a straight vertical line at $x = 0$ on the force-displacement curve. At ultra-high loads ($F/R > 2200$ mN/m), the curve deviates from a straight line. This effect has been observed when collecting high-load force curves and is attributed to a buckling of the cantilever in the vicinity of the reflected laser spot (Hoh and Engel, 1993). Buckling effects divert the reflected laser spot back toward the center of the detector, causing the true deflection to be underestimated. This is manifested as an abrupt deviation from linearity in the force curve. The degree of cantilever buckling at a given load is a function of cantilever spring constant and geometry (Warmack et al., 1994). The use of longer, less stiff cantilevers to probe LB layers leads to buckling at loads lower than $F/R = 1000$ mN/m, distorting the data and preventing an accurate detector calibration. Buckling effects can greatly affect both topographic and friction images (Warmack et al., 1994). Therefore, all images presented here were collected at loads below the onset of buckling, as judged by force-displacement curves.

CONCLUSIONS

We have combined information from AFM force curves and images of phase-separated mixed monolayers of DSPE/DOPE and MGDG/DOPE to explain the molecular mechanisms responsible for the topographic imaging contrast observed in these systems. By control of the AFM probe chemistry and thorough characterization of the probe radius and cantilever spring constant, we have shown that a breakthrough force exists that is a repeatable, material-dependent quantity. When imaging phase-separated lipid layers at a force between the breakthrough forces of each phase, topography contrast is obtained by preferential penetration of one phase. The topography contrast is removed when imaging above the breakthrough force of both phases. Frictional contrast is highest for penetrated domains; when comparing two penetrated domains, that with the highest critical shear stress has the highest friction. These results provide a framework for the analysis of AFM force curves. This analysis should be conducted before imaging lipid films to establish an appropriate set point for imaging. AFM force curves interpreted using this method could also serve as a powerful quantitative probe of membrane/water interfacial chemistry.

This work was supported by the Office of Naval Research. J. W. S. was supported by a postdoctoral fellowship from the American Society for Engineering Education. We thank David Allara for providing the alkanethiols and John-Bruce Green and Thomas Boland for valuable discussions.

REFERENCES

- Bain, C. D., E. B. Troughton, Y. T. Tao, J. Evall, G. M. Whitesides, and R. G. Nuzzo. 1989. Formation of monolayer films by the spontaneous assembly of organic thiols from solution onto gold. *J. Am. Chem. Soc.* 111:321–335.
- Berridge, M. J., and R. F. Irvine. 1984. Inositol trisphosphate, a novel second messenger in cellular signal transduction. *Nature.* 312:315–321.
- Blackman, G. S., C. M. Mate, and M. R. Philpott. 1990. Interaction forces of a sharp tungsten tip with molecular films on silicon surfaces. *Phys. Rev. Lett.* 65:2270–2273.
- Boland, T., Y. Dufrene, W. R. Barger, and G. U. Lee. 1999. Characterization of hybrid lipid bilayers with atomic force microscopy. *Proc. Southern Biomed. Conf.* (in preparation).
- Bowden, F. P., and D. Tabor. 1967. Friction and Lubrication. John Wiley and Sons, New York.
- Buchailot, L., E. Farnault, M. Hoummady, and H. Fujita. 1997. Silicon nitride thin films Young's modulus determination by an optical non destructive method. *Jpn. J. Appl. Phys.* 36:L794–L797.
- Butt, H. J. 1991a. Electrostatic interaction in atomic force microscopy. *Biophys. J.* 60:777–785.
- Butt, H. J. 1991b. Measuring electrostatic, van der Waals, and hydration forces in electrolyte solutions with an atomic force microscope. *Biophys. J.* 60:1438–1444.
- Chi, L. F. 1999. Applications of scanning force microscopy operating in dynamic modes on self-organized assemblies of nanoclusters and organic amphiphiles. *Appl. Phys. A.* 68:203–210.
- Chi, L. F., M. Anders, H. Fuchs, R. R. Johnston, and H. Ringsdorf. 1993. Domain structures in Langmuir-Blodgett films investigated by atomic force microscopy. *Science.* 259:213–216.
- Cornell, B. A., V. L. B. Braach-Maksvytis, L. B. King, P. D. J. Osman, B. Raguse, L. Wiczorek, and R. J. Pace. 1997. A biosensor that uses ion-channel switches. *Nature.* 387:580–583.
- Derjaguin, B. 1934. Untersuchungen über die reibung und adhäsion, IV. *Kolloid-Zeits.* 69:155–164.
- Discher, B. M., K. M. Maloney, W. R. Schief, D. W. Grainger, V. Vogel, and S. B. Hall. 1996. Lateral phase separation in interfacial films of pulmonary surfactant. *Biophys. J.* 71:2583–2590.
- Domke, J., and M. Radmacher. 1998. Measuring the elastic properties of thin polymer films with the atomic force microscope. *Langmuir.* 14:3320–3325.
- Ducker, W. A., and D. R. Clarke. 1994. Controlled modification of silicon nitride interactions in water via zwitterionic surfactant adsorption. *Coll. Surf. A.* 94:275–292.
- Dufrène, Y. F., W. R. Barger, J. D. Green, and G. U. Lee. 1997. Phase-separated phospholipid monolayers and bilayers studied by atomic force microscopy. *Langmuir.* 13:4779–4784.
- Dufrène, Y. F., T. Boland, J. W. Schneider, W. R. Barger, and G. U. Lee. 1998. Characterization of the physical properties of model biomembranes at the nanometer scale with the atomic force microscope. *Faraday Disc.* 111:79–94.
- Grotenhuis, E. t., R. A. Demel, M. Ponec, D. R. Boer, J. C. v. Miltenburg, and J. A. Bouwstra. 1996. Phase behavior of stratum corneum lipids in mixed Langmuir-Blodgett monolayers. *Biophys. J.* 71:1389–1399.
- Hainsworth, S. V., T. Bartlett, and T. F. Page. 1993. The nanoindentation response of systems with thin hard carbon coatings. *Thin Solid Films.* 236:214–218.
- Hammer, D. A., and M. Tirrell. 1996. Biological adhesion at interfaces. *Annu. Rev. Mater. Sci.* 26:651–691.
- Hansma, H. G., S. A. C. Gould, P. K. Hansma, H. E. Gaub, M. L. Longo, and J. A. N. Zasadzinski. 1991. Imaging nanometer scale defects in Langmuir-Blodgett films with the atomic force microscope. *Langmuir.* 7:1051–1054.
- Helm, C. A., J. N. Israelachvili, and P. M. McGuiggan. 1989. Molecular mechanisms and forces involved in the adhesion and fusion of amphiphilic bilayers. *Science.* 246:919–922.
- Helm, C. A., J. N. Israelachvili, and P. M. McGuiggan. 1992. Role of hydrophobic forces in bilayer adhesion and fusion. *Biochemistry.* 31:1794–1805.
- Ho, R., J.-Y. Yuan, and Z. Shao. 1998. Hydration force in the atomic force microscope: a computational study. *Biophys. J.* 75:1076–1083.
- Hoh, J. H., and A. Engel. 1993. Friction effects on force measurements with an atomic force microscope. *Langmuir.* 9:3310–3312.
- Hui, S. W., R. Viswanathan, J. A. Zasadzinski, and J. N. Israelachvili. 1995. The structure and stability of phospholipid bilayers by atomic force microscopy. *Biophys. J.* 68:171–178.
- Johnson, K. L. 1985. Contact Mechanics. Cambridge University Press, New York.
- Koleske, D. D., W. R. Barger, G. U. Lee, and R. J. Colton. 1997. Scanning probe microscope study of mixed chain-length phase-segregated Langmuir-Blodgett monolayers. *Mat. Res. Soc. Symp. Proc.* 464:377–380.
- Lee, G. U., L. A. Chrisey, C. E. O'Ferrall, D. E. Pilloff, N. H. Turner, and R. J. Colton. 1996. Chemically-specific probes for the atomic force microscope. *Isr. J. Chem.* 36:81–87.
- Leporatti, S., S. Akari, F. Bringezu, G. Brezesinski, and H. Mohwald. 1998. Triple-chain phospholipid monolayers: a scanning force microscopy and grazing incidence x-ray diffraction study. *Appl. Phys. A.* 66:S1245–S1249.
- Lipp, M. M., K. Y. C. Lee, A. Waring, and J. A. Zasadzinski. 1997. Fluorescence, polarized fluorescence, and Brewster angle microscopy of palmitic acid and lung surfactant protein B monolayers. *Biophys. J.* 72:2783–2804.
- Manne, S., J. P. Cleveland, H. E. Gaub, G. D. Stucky, and P. K. Hansma. 1994. Direct visualization of surfactant hemimicelles by force microscopy of the electric double layer. *Langmuir.* 10:4409–4413.
- Manne, S., and H. E. Gaub. 1995. Molecular organization of surfactants at solid-liquid interfaces. *Science.* 270:1480–1482.

- Marra, J., and J. Israelachvili. 1985. Direct measurement of forces between phosphatidylcholine and phosphatidylethanolamine bilayers in aqueous electrolyte solutions. *Biochemistry*. 24:4608–4618.
- McConnell, H. M., T. H. Watts, R. M. Weis, and A. A. Brian. 1986. Supported planar membranes in studies of cell-cell recognition in the immune system. *Biochim. Biophys. Acta*. 864:95–106.
- Meijers, P. 1968. The contact problem of a rigid cylinder on an elastic layer. *Appl. Sci. Res.* 18:353–383.
- Meine, K., D. Vollhardt, and G. Weidemann. 1998. Atomic force microscopy study of the texture of condensed phase domains in 1-monostearoylglycerol monolayers. *Langmuir*. 14:1815–1821.
- Nahmen, A. v., M. Schenk, M. Sieber, and M. Amrein. 1997. The structure of a model pulmonary surfactant as revealed by scanning force microscopy. *Biophys. J.* 72:463–469.
- Ogilvy, J. A. 1993. A parametric elastic model for indentation testing of thin films. *J. Phys. D: Appl. Phys.* 26:2123–2131.
- Overney, R. M., E. Meyer, J. Frommer, D. Brodbeck, R. Luthi, L. Howald, H.-J. Guntherodt, M. Fujihara, H. Takano, and Y. Gotoh. 1992. Friction measurements on phase-separated thin films with a modified atomic force microscope. *Nature*. 359:133–135.
- Parsegian, V. A. 1966. Theory of liquid-crystal phase transitions in lipid + water systems. *Trans. Faraday Soc.* 62:848–860.
- Plant, A. L. 1999. Supported hybrid bilayer membranes as rugged cell membrane mimics. *Langmuir*. 15:5128–5135.
- Radler, J., M. Radmacher, and H. E. Gaub. 1994. Velocity-dependent forces in atomic force microscopy imaging of lipid films. *Langmuir*. 10:3111–3115.
- Radmacher, M., M. Fritz, and P. K. Hansma. 1995. Imaging soft samples with the atomic force microscope: gelatin in water and propanol. *Biophys. J.* 69:264–270.
- Sackmann, E. 1996. Supported membranes: scientific and practical applications. *Science*. 271:43–48.
- Salmeron, M., G. Neubauer, A. Folch, M. Tomitori, D. F. Ogletree, and P. Sautet. 1993. Viscoelastic and electrical properties of self-assembled monolayers on Au(111) films. *Langmuir*. 9:3600–3611.
- Schaper, A., L. Wolthaus, D. Mobius, and T. M. Jovin. 1993. Surface morphology and stability of Langmuir-Blodgett mono- and multilayers of saturated fatty acids by scanning force microscopy. *Langmuir*. 9:2178–2184.
- Schwartz, D. K., J. Garnaes, R. Viswanathan, and J. A. N. Zasadzinski. 1992. Surface order and stability of Langmuir-Blodgett films. *Science*. 257:508–511.
- Seddon, J. M., G. Cevc, R. D. Kaye, and D. Marsh. 1984. X-ray diffraction study of the polymorphism of hydrated diacyl and dialkylphosphatidylethanolamines. *Biochemistry*. 23:2634–2644.
- Shieko, S. S., M. Moller, E. M. C. M. Reuvekamp, and H. W. Zandbergen. 1993. Calibration and evaluation of scanning-force-microscopy probes. *Phys. Rev. B*. 48:5675–5678.
- Solletti, J. M., M. Botreau, F. Sommer, T. M. Duc, and M. R. Celio. 1996. Characterization of mixed miscible and nonmiscible phospholipid Langmuir-Blodgett films by atomic force microscopy. *J. Vac. Sci. Tech.* 14:1492–1497.
- Stedfeld, R. 1979. *Mater. Eng.* 90:C120–C130.
- Stelzle, M., G. Weissmuller, and E. Sackmann. 1993. On the application of supported bilayers as receptive layers for biosensors for electrical detection. *J. Phys. Chem.* 97:2974–2981.
- Tortonesi, M., and M. Kirk. 1997. Characterization of application specific probes for SPMs. *SPIE*. 3009:53–60.
- Vie, V., N. V. Mau, E. Lesniewska, J. P. Goudonnet, F. Heitz, and C. L. Grimallec. 1998. Distribution of ganglioside GM1 between two-component, two-phase phosphatidylcholine monolayers. *Langmuir*. 14:4574–4583.
- Voet, D., and J. G. Voet. 1990. *Biochemistry*. John Wiley and Sons, New York.
- Warmack, R. J., X. Y. Zheng, T. Thundat, and D. P. Allison. 1994. Friction effects in the deflection of atomic-force microscope cantilevers. *Rev. Sci. Instrum.* 65:394–399.
- Weisenhorn, A. L., M. Egger, F. Ohnesorge, S. A. C. Gould, S.-P. Heyn, H. G. Hansma, R. L. Sinsheimer, H. E. Gaub, and P. K. Hansma. 1991. Molecular-resolution images of Langmuir-Blodgett films and DNA by atomic force microscopy. *Langmuir*. 7:8–12.
- Yu, Y. C., T. Pakalns, Y. Dori, J. B. McCarthy, M. Tirrell, and G. B. Fields. 1997. Construction of biologically active protein molecular architecture using self-assembly. *Methods Enzymol.* 289:571–587.
- Zasadzinski, J. A. N., C. A. Helm, M. L. Longo, A. L. Weisenhorn, S. A. C. Gould, and P. K. Hansma. 1991. Atomic force microscopy of hydrated phosphatidylethanolamine bilayers. *Biophys. J.* 69:755–760.